

Article

Structural Design of Dry-Processed Lithium-Rich Mn-Based Materials with High Loading for Enhanced Energy Density

Yujie Ma, Haojin Guo, Tai Yang * and Zhifeng Wang *

School of Materials Science and Engineering, Hebei University of Technology, Tianjin 300401, China; 202231802015@stu.hebut.edu.cn (Y.M.); 202221801135@stu.hebut.edu.cn (H.G.)

* Correspondence: yangtai@hebut.edu.cn (T.Y.); wangzf@hebut.edu.cn (Z.W.); Tel.: +86-22-60204129 (T.Y.); +86-22-60202006 (Z.W.)

Abstract: With the growing demand for electric vehicles and consumer electronics, lithium-ion batteries with a high energy density are urgently needed. Lithium-rich manganese-based materials (LRMs) are known for their high theoretical specific capacity, rapid electron/ion transfer, and high output voltage. Constructing electrodes with a substantial amount of active materials is a viable method for enhancing the energy density of batteries. In this study, we prepare thick LRM electrodes through a dry process method of binder fibrillation. A point-to-line-to-surface three-dimensional conductive network is designed by carbon agents with various morphologies. This structural design improves conductivity and facilitates efficient ion and electron transport due to close particle contact and tight packing. A high-loading cathode (35 mg cm^{-2}) is fabricated, achieving an impressive areal capacity of up to 7.9 mAh cm^{-2} . Moreover, the pouch cell paired with a lithium metal anode exhibits a remarkable energy density of 949 Wh kg^{-1} . Compared with the cathodes prepared by the wet process, the dry process optimizes the pathways for e^-/Li^+ transport, leading to reduced resistance, superior coulombic efficiency, retention over cycling, and minimized side reaction. Therefore, the novel structural adoption of the dry process represents a promising avenue for driving innovation and pushing the boundaries for enhanced energy density for batteries.



Academic Editor: Dino Tonti

Received: 26 February 2025

Revised: 4 April 2025

Accepted: 5 April 2025

Published: 7 April 2025

Citation: Ma, Y.; Guo, H.; Yang, T.; Wang, Z. Structural Design of Dry-Processed Lithium-Rich Mn-Based Materials with High Loading for Enhanced Energy Density. *Batteries* **2025**, *11*, 146. <https://doi.org/10.3390/batteries11040146>

Copyright: © 2025 by the authors. Licensee MDPI, Basel, Switzerland. This article is an open access article distributed under the terms and conditions of the Creative Commons Attribution (CC BY) license

(<https://creativecommons.org/licenses/by/4.0/>).

Keywords: Li-ion battery; Li-rich Mn-based materials; cathode; energy density

1. Introduction

Lithium-ion batteries (LIBs) have become the leading energy storage technology due to their outstanding properties, such as a high energy density, superior power output, extended cycle life, and exceptional reliability [1–3]. As global demand continues to surge, increasing energy density has become a paramount challenge for the battery industry [4]. However, the energy density of commercial cathode materials has largely plateaued, highlighting the urgent need for innovations in manufacturing processes. By advancing process engineering, it is possible to achieve breakthroughs in efficiency, scalability, and performance, paving the way for developing batteries with even greater capacity and power [5]. One promising approach to enhancing energy density is the development of electrodes with a higher proportion of active materials. This strategy reduces the reliance on non-active components, such as separators and conductive additives, thereby maximizing the energy storage potential of LIBs [6,7].

The conventional wet processing technique frequently faces challenges in handling thick electrodes, especially during the solvent evaporation stage. This process may lead to

several issues, like the non-uniform distribution of binders and conductive carbon materials [8]. N-methyl-2-pyrrolidone (NMP), widely employed as a solvent in the wet processing of mixing cathode composites, presents environmental and economic challenges due to its evaporation and recycling [9,10]. Dry electrode technology signifies a transformative advancement in energy storage manufacturing, delivering substantial advantages that extend far beyond process simplification and environmental footprint reduction. By obviating the requirement for solvents, dry electrode fabrication substantially mitigates operational hazards and ecological risks. This solvent-free approach contributes to safer and more sustainable battery production. Additionally, the inherent scalability and cost-effectiveness of dry processing techniques make them well suited for large-scale production, facilitating the widespread adoption of energy storage solutions across various industries [11,12].

Dry processing techniques are particularly well suited for constructing electrodes with a high loading of active materials, which has been widely studied by researchers [13]. While Tesla has successfully implemented dry processing for anode fabrication, technical hurdles persist in cathode adaptation due to PTFE fibrillation challenges. During the process of binder fibrillation, the active materials, conductive carbon, and binder polytetrafluoroethylene (PTFE) are mixed to achieve uniform dispersion. During shear processing, PTFE undergoes microstructural transformation from spherical particles to interconnected fibrils that form percolating networks. These nanofibrils mechanically interlock active material particles with conductive carbon additives, achieving greater improvements [14–16].

Layered lithium-rich manganese-based materials (LRMs) have emerged as promising next-generation cathode candidates for LIBs due to their high specific capacity ($>250 \text{ mAh g}^{-1}$) and low cost [17]. This study employs LRM as a cathode active material, synergistically integrating three conductive additives: Super C65 carbon black, vapor-grown carbon fibers (VGCFs), and graphene nanosheets. By constructing a point-to-line-to-surface three-dimensional conductive network, the intimate contact between the active material particles and the conductive carbon particles is significantly enhanced. This intricate network architecture facilitates efficient charge transfer pathways, minimizes electron transport resistance, and maximizes the utilization of active materials. The LRM cathodes prepared by the binder fibrillation process were adjusted to various thickness and mass loadings ranging from 15 mg cm^{-2} to 35 mg cm^{-2} . These cathodes exhibited a high areal density of 7.9 mAh cm^{-2} and a remarkable energy density of 949 Wh kg^{-1} . Compared with the wet process, the dry-processed cathodes optimize the pathways for e^-/Li^+ transport. This optimization leads to reduced resistance, superior Coulombic efficiency, enhanced retention over cycling, and minimized side reactions.

2. Materials and Methods

2.1. Preparation of Electrode

The synthetic route of the LRM can be found in Supporting S1 [18]. The cathode composite was formulated by integrating lithium-rich manganese-based oxide with a ternary conductive system (C65:graphene:VGCF = 1:1:4 *w/w*) and polytetrafluoroethylene (PTFE) binder at precisely controlled mass ratios of 90:6:4, and then 200 °C drying for 1 h. The mixed material was rolled into film by a roller several times until it became a dense self-supporting film. The areal loadings of the self-supporting films with a thickness of 60 μm , 100 μm and 130 μm are 15 mg cm^{-2} , 25 mg cm^{-2} and 35 mg cm^{-2} , respectively. For comparison, the electrode prepared via the wet process was composed of LRM, a composite conductive agent (C65:graphene:VGCF = 1:1:4), and polyvinylidene fluoride (PVDF) according to the mass ratio of 90:6:4.

2.2. Material Characterization

The electrode morphology was characterized using a scanning electron microscope (SEM, Zeiss Merlin, Bochum, Germany) at an acceleration voltage of 5 kV. Surface chemistry analysis was performed by X-ray photoelectron spectra (XPS, ESCALAB 250Xi, Waltham, MA, USA) featuring a monochromatic Al K α (1486.6 eV) X-ray source, focused on a 400 μm spot under a vacuum pressure lower than 1×10^{-7} mbar. Contact angle measurements were performed with a KRUSS DSA100 (Hamburg, Germany). The structural changes of the cathode, both before and after cycling, were analyzed by X-ray diffraction (XRD, Rigaku D8 Discover, Karlsruhe, Germany) using a PANalytical Empyrean Series 2 equipped with a Cu K α radiation source (45 kV, 40 mA). The electrical resistivity of the electrodes was measured using an IEST BER2500 (Xiamen, China). For large-area cross-sectional milling and subsequent SEM imaging, a Thermo Scientific Helios 5 Hydra Plasma Focused Ion Beam (PFIB) DualBeam system (Göteborg, Sweden) was utilized. Cross-sections of various electrode samples were milled and cleaned using a Xe $^+$ ion source. High-resolution transmission electron microscopy (HRTEM) images of both pristine and cycled samples were acquired using a ThermoFisher Talos F200X (Waltham, MA, USA), equipped with a Ceta camera and operated at 200 kV. BET analysis of various particles was conducted using a gas adsorption/surface area analyzer (Micromeritic ASAP 2020, Atlanta, GA, USA). The TOF-SIMS (time-of-flight secondary ion mass spectrometry) measurements were performed using TOF-SIMS 5-100 (IONTOF, Ingolstadt, Germany) with a primary ion beam of Bi $^{3+}$ and sputtering ion beam of Cs $^+$.

2.3. Electrochemical Measurements

Electrochemical performance was evaluated in an argon-filled glove box using 2032-type coin cells with a Li metal anode, polyethylene (PE) separator, and Shanshan 003 liquid electrolyte. Cell performance was tested within the 2.0–4.8 V vs. Li/Li $^+$ range. The cycling test was carried out under various charging/discharging conditions. EIS and CV were performed using an electrochemical workstation (Interface 1010E, Gamry Instruments, Philadelphia, PA, USA). The lithium metal pouch cell was assembled with a 100 μm lithium metal anode in a dry room at a –50 °C dew point.

3. Results and Discussion

Figure 1 illustrates a schematic diagram of the binder fibrillation process. During the process, LRM, conductive carbon, and PTFE are mixed, followed by the induction of fibrillation of PTFE under shear force. The resulting fibers, with diameters of only a few nanometers and lengths of tens of micrometers, form a three-dimensional network structure that aggregates the active material and carbon black (Supplementary Materials, Figure S1). Subsequently, this mixture is compressed between two rollers to form films of varying thickness. The conductive agent plays a critical role in electrode performance. Its type and content can influence the flexibility and mechanical strength of the electrode, thereby affecting the battery's flexibility and durability. The conductive agent also possesses excellent electrical conductivity, facilitating electron transport within the electrode, which reduces internal resistance and improves overall conductivity. Additionally, the conductive agent helps to form a conductive network, establishing effective electron transfer pathways between the active material and the electrode substrate, thereby enhancing the electrode's structure, stability, and cycling life. Therefore, when designing electrodes, we selected different carbon and carbon composites to optimize performance. As shown in Table S1, we performed a series of control tests with different carbon ratios, and the four ratios were determined based on the integrity and flexibility of film during the preparation process. As shown in Figure S2, the carbon composites of VGCF, C65, and graphene with the mass ratio

of 4:1:1 demonstrated higher conductivity than single VGCF, VGCF and C65 (mass ratio of 5:1), and VGCF and graphene (mass ratio of 5:1). Therefore, the point-to-line-to-surface three-dimensional conductive network facilitated efficient electron transport throughout the cathodes and enhanced overall conductivity.

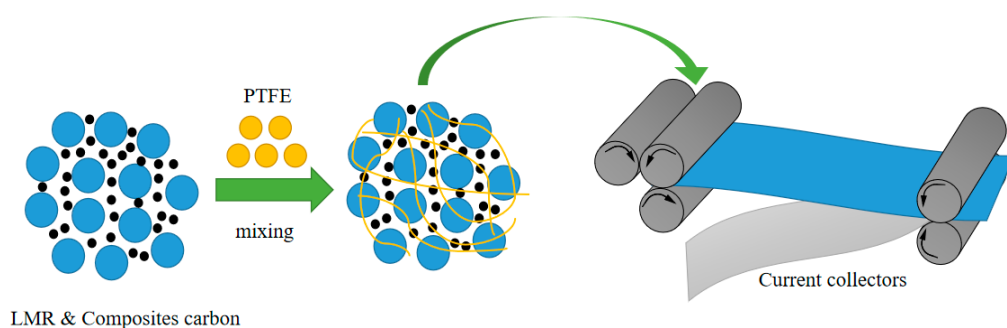


Figure 1. The schematic diagram of the binder fibrillation process.

Figure 2 illustrates the cross-section topography of LRM electrodes with varying thicknesses (60, 100, 130 μm). It is evident that LRM particles, carbon, and PTFE are closely intertwined, forming a cohesive and conductive framework. As shown in Figure S3, the XRD patterns of the LRM raw materials and dry-processed electrodes are consistent, indicating that the macroscopic crystal structure is maintained. This suggests that the dry-processing method has a minimal impact on the material's structure and may offer advantages in terms of structural stability. This fibrous structure provides excellent mechanical support and conductive pathways for the electrode, enhancing its stability and electrochemical performance. As the electrode thickness decreases, a finer and more interconnected network of fibers is observed throughout the electrode. This tighter integration improves electrical conductivity and facilitates efficient charge transfer. Additionally, the reduced thickness brings the electrode components closer together, maximizing their interaction and synergistic effects. The rolling process is effective in controlling the porosity and compaction density of the cathodes. As shown in Figure S4, increasing thickness results in lower compaction density and higher porosity. Contact angle results (Figure 2c,f,i) indicate that, as the thickness decreases, the contact angle increases, reducing wettability. To optimize wettability, we proactively increased the volume of electrolytes during the battery assembly process. Firstly, we completely flooded the cathodes with electrolytes for 2 h before assembling the cell, and then we added 150 μl of electrolytes to assemble the cell to ensure a sufficient amount of electrolytes during the measurement. By doing so, we aimed to improve the penetration and coverage of the electrode surface, enhancing the electrolyte–electrode interaction. This adjustment not only promotes efficient ion transport within the electrode but also improves electrochemical performance by minimizing electrolyte depletion and ensuring adequate contact between the electrolyte and active materials. Additionally, optimizing electrolyte volume helps to address reduced wettability due to higher electrode packing densities, ensuring consistent and reliable battery performance under various operating conditions.

The rate and cycle performances of the Li-rich manganese material were tested, with the results shown in Figure 3 (1 C = 200 mAh g^{-1}). At a current rate of 0.1 C, the cathode with a mass loading of 15 mg cm^{-2} achieved an initial discharge capacity of 270 mAh g^{-1} . Increasing the mass loading to 25 and 35 mg cm^{-2} resulted in initial discharge capacities of 250 mAh g^{-1} and 226 mAh g^{-1} , respectively (Figure 3a). Consequently, a high areal capacity of 7.9 mAh cm^{-2} was achieved with a mass loading of 35 mg cm^{-2} . During rate testing from 0.1 C to 2 C, the electrode with a mass loading of 15 mg cm^{-2} demonstrated significantly superior rate capability compared to the others (Figure 3b). As shown in Figure 3c,

after 20 cycles, the electrode with a 15 mg cm^{-2} loading exhibited a capacity retention rate of 87.8%, outperforming the electrodes with 25 mg cm^{-2} (81.1%) and 35 mg cm^{-2} (63.3%) loadings. The cycling stability exhibited an inverse correlation with electrode mass loading, as evidenced by a more pronounced capacity degradation in higher-loading samples. Notably, the cathode fabricated with a mass loading of 15 mg cm^{-2} demonstrated 65% capacity retention after 100 charge/discharge cycles (Figure S5). It was found that, under low-rate discharge conditions, electrode thickness has a minimal effect on battery efficiency. However, as the electrode thickness increases and discharge rates rise, battery efficiency declines. The rate capability of the battery decreases with both increasing electrode thickness and higher discharge rates. A Li || LRM pouch cell was assembled using Li metal ($100 \mu\text{m}$) and LRM (25 mg cm^{-2}) (Figure S6).

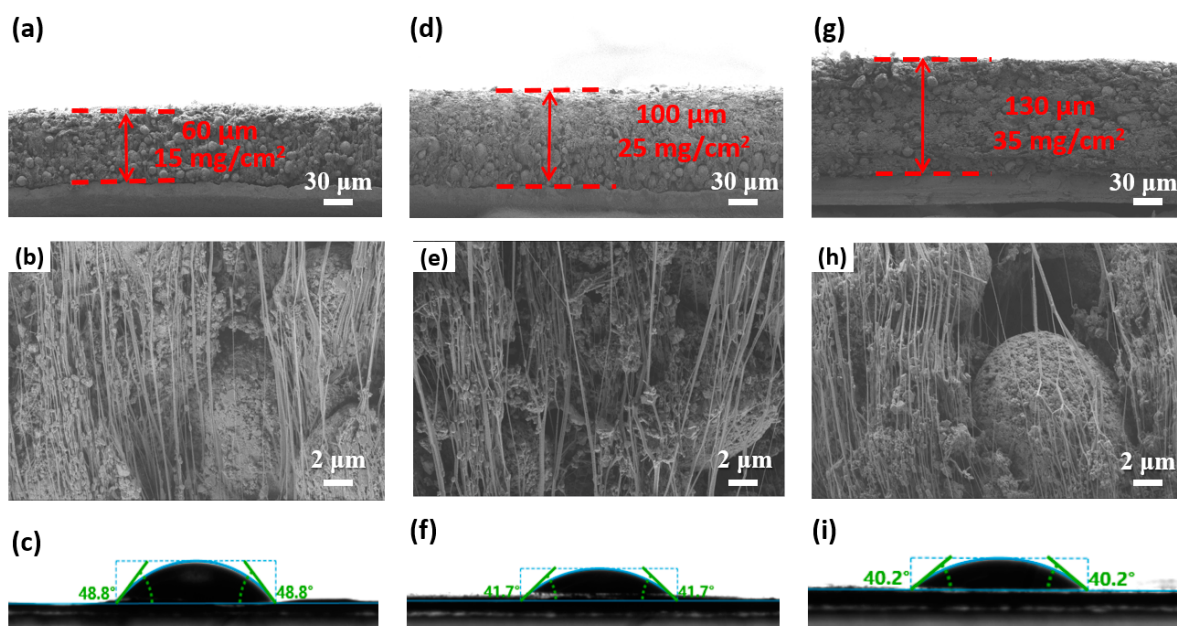


Figure 2. Cross-section SEM images (a,d,g), SEM images (b,e,h) and Contact angles (c,f,i) of LRM with various mass loading.

The pouch cell exhibited an initial discharge capacity of 300 mAh g^{-1} at 0.1 C , corresponding to an energy density of 949 Wh kg^{-1} . We investigated the impact of thickness on efficiency and rate capability using time-of-flight secondary ion mass spectrometry (TOF-SIMS) analysis of cycled cathodes (Figure 3d). Interactions with organic electrolytes lead to surface structural degradation inside the cathodes [19,20]. The quantities of F^- , PO_4^{2-} , and C_2HO^- species identified in the cathodes with 15 mg cm^{-2} were significantly lower compared to those with 25 and 35 mg cm^{-2} [21].

SEM images of the electrodes after cycling reveal a clear trend: as the thickness of the electrodes increases, the presence of surface cracks becomes more pronounced (Figure 4). This provides additional evidence of the heightened occurrence of side reactions in thicker electrodes. Cracks on the electrode surface provide penetration paths for the electrolyte, allowing the electrolyte to more readily access the interior of the electrode material, thus exacerbating side reactions at the electrode/electrolyte interface [22–24]. The cracks can compromise the structural integrity of the electrode, contributing to higher impedance and reduced cycling stability, as confirmed by the tests.

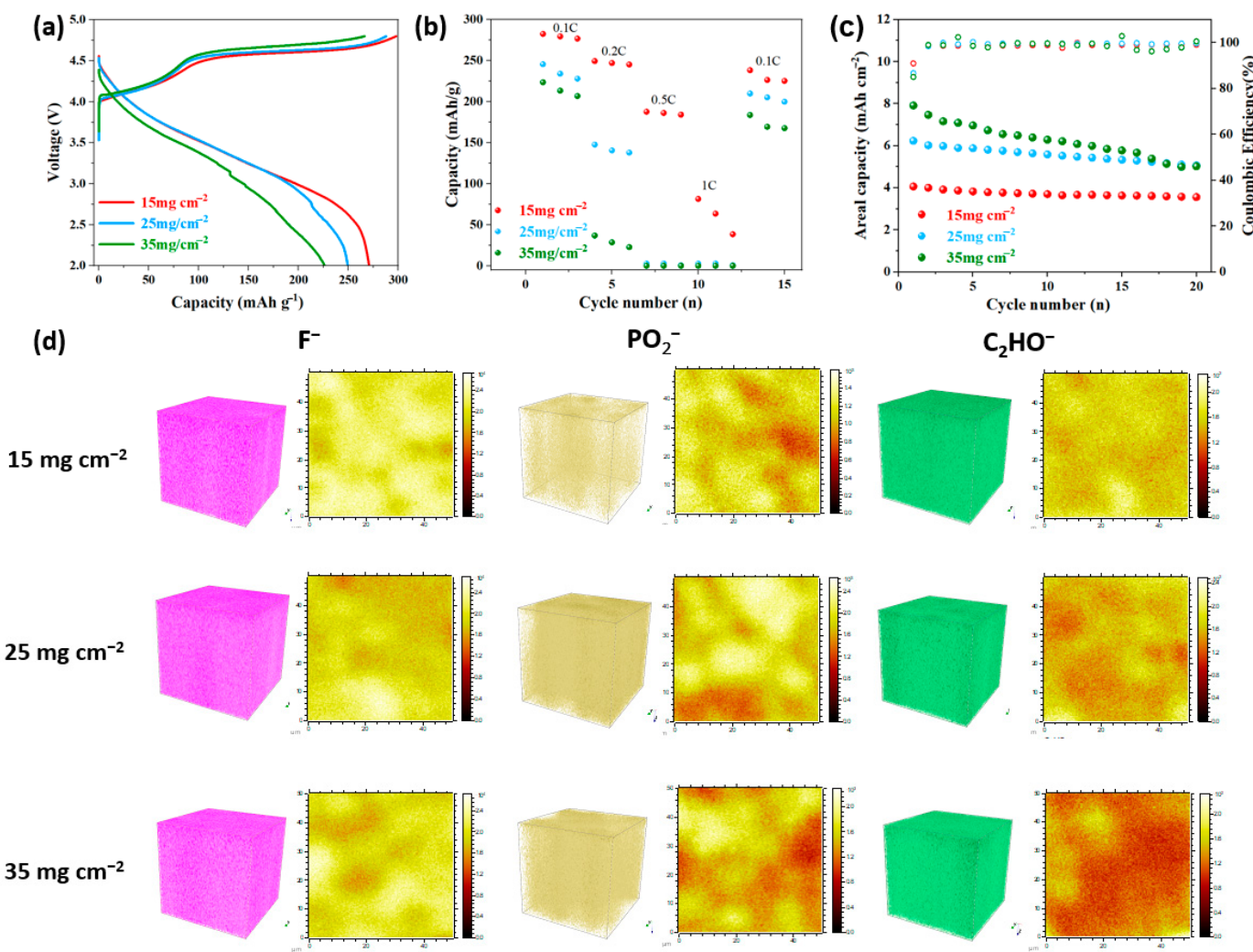


Figure 3. (a) Charge/discharge voltage profiles, (b) rate capability performance, (c) cycling performance of cathodes with various mass loadings at 0.1C and a voltage range of 2.0–4.8 V. (d) The 3D views and chemical imaging for F^- , PO_4^{2-} , and CH_2O^- of cycled cathodes.

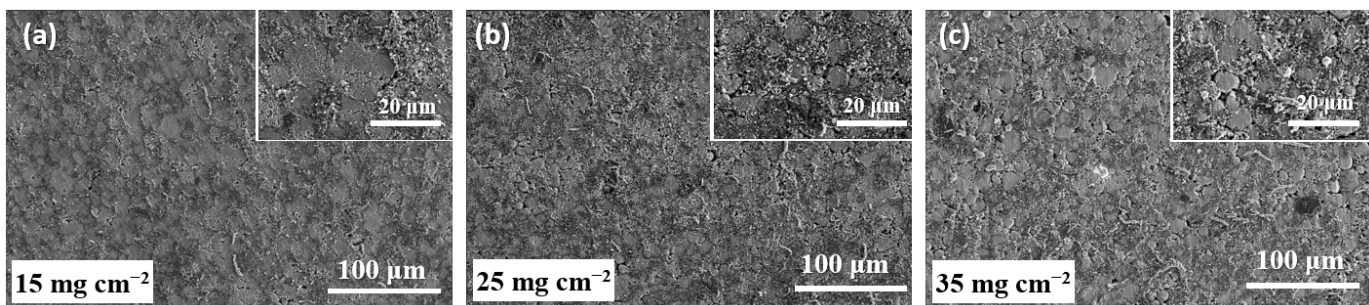


Figure 4. SEM of cycled cathodes with various mass loadings: (a) 15 mg cm^{-2} , (b) 25 mg cm^{-2} , (c) 35 mg cm^{-2} .

As electrode thickness increases, there is enhanced infiltration of the electrolyte into the electrode structure; this suggests that the infiltration may lead to an increase in secondary reactions within the electrode, which could negatively impact battery performance and cycling stability. For thick electrode batteries, transport limitations of the electrolyte and ohmic polarization are the primary factors limiting efficiency at high discharge rates [25]. An et al. demonstrated the spatial distribution of Li^+ at the end of discharge in cathodes with various thicknesses using a granular stacking model [26]. The results showed that

the gradient of Li⁺ concentration becomes more pronounced as areal density increases. In thick cathodes with high areal density, the active material particles exhibit uneven sizes. Li⁺ tends to diffuse more rapidly within smaller particles, leading to significant irregularities in the distribution of Li⁺ concentration. The uneven distribution of Li⁺ results in inconsistent discharge depths among active particles, further affecting the performance and efficiency of the battery.

We compared the performance of cathodes prepared by the dry process and wet process, as shown in Figure 5. The electrochemical impedance spectroscopy (EIS) results (Figure 5a) further show that the dry-process cathode exhibits lower impedance compared to the wet-process cathode, resulting in tighter interfacial contact between particles. This forms more efficient ion transport pathways, thereby reducing interfacial contact resistance and minimizing energy loss during ion transport. In contrast, in wet-processed electrodes, the presence of solvent may lead to uneven distribution between the active material and conductive agent. After solvent evaporation, interfacial defects are formed, leaving discontinuous ion transport pathways, which ultimately reduce ion transport efficiency [27]. The cycling performance (Figure 5b) shows that the discharge specific capacity of dry film is slightly lower than that of the wet film. However, the dry film demonstrates a higher initial Coulombic efficiency, indicating more efficient utilization of the active material. Additionally, the dry film shows a capacity retention rate of 84.5%, which is higher than the wet film (83.6%). The comparison of dQ/dV curves between the dry film (Figure 5c) and wet film (Figure 5d) reveals that the dry film exhibits a more stable performance [28,29], consistent with the cycling test results.

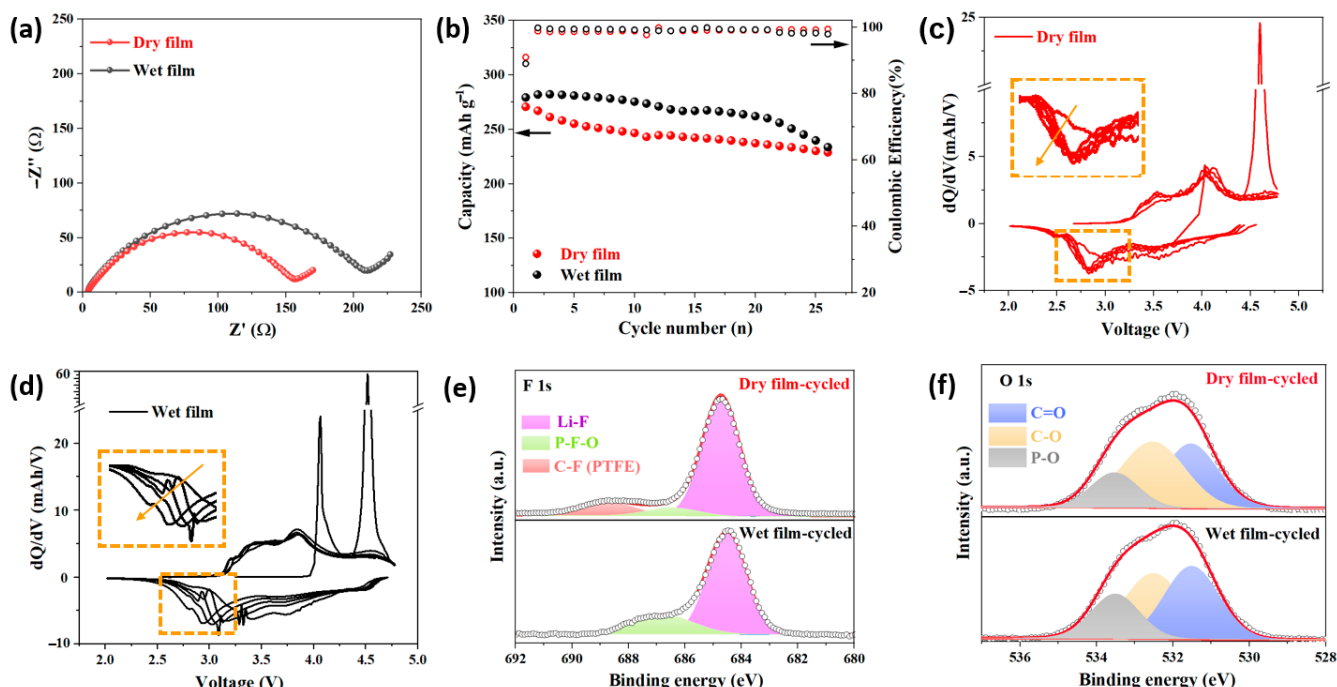


Figure 5. (a) EIS results, (b) cycling performance of dry film and wet film. dQ/dV curves of (c) dry film and (d) wet film. (e) F 1s, and (f) O 1s core spectra of cycled dry film and wet film.

To gain insight into the structural improvements that contribute to the dry film's enhanced battery performance, we analyzed the composition of the cathode electrolyte interphase (CEI). We retrieved the cathodes of both dry-film and wet-film cells after formation for XPS characterization. The F 1s spectrum (Figure 5e) reveals a higher presence of LiF (79.7% vs. 77.4%) on the surface of the dry film, indicating the formation of a robust LiF-rich CEI as a protective layer that efficiently inhibits unwanted side reactions between

the cathode and the electrolyte [30]. Additionally, the O 1s spectrum (Figure 5f) shows a higher proportion of P-O (22.08% vs. 17.10%) on the surface of the wet film, suggesting more side reactions with organic electrolytes, which leads to surface structural degradation. These results indicate that the network structure of the dry film optimizes ion transport and electron conduction pathways, resulting in reduced resistance and superior Columbic efficiency and retention over cycling. This highlights the superior utilization of active materials in the dry film, potentially due to its more effective structural integrity and minimized side reactions during operation [31,32]. In contrast, the wet film exhibited higher impedance due to the formation of clusters or less uniform distribution of active materials and binders, which hinders efficient e^-/Li^+ transfer and contributes to increased side reactions with electrolytes.

The SEM image (Figure S7) of the wet film reveals that the active material, carbon materials, and PVDF binder aggregate into clusters. In contrast, the dry film forms a three-dimensional conductive network that reduces polarization effects and enhances charge transfer efficiency (Figure S1). To ensure the accuracy of the comparison results, we selected dry and wet cathodes with similar mass loadings (Figure 6). According to the porosity formula [33], dry films have lower porosity than wet films (30% vs. 43%). It is noteworthy that PTFE is typically used in dry-processed electrodes, whereas PVDF is commonly employed in wet-processed electrodes, as this pairing is dictated by their respective processing requirements. The choice of binder significantly influences the SEI composition, the electrode structure, and, consequently, the electrochemical cycling performance. This inherent constraint reveals the intricate relationship between binder chemistry and electrode fabrication methods in determining overall battery performance.

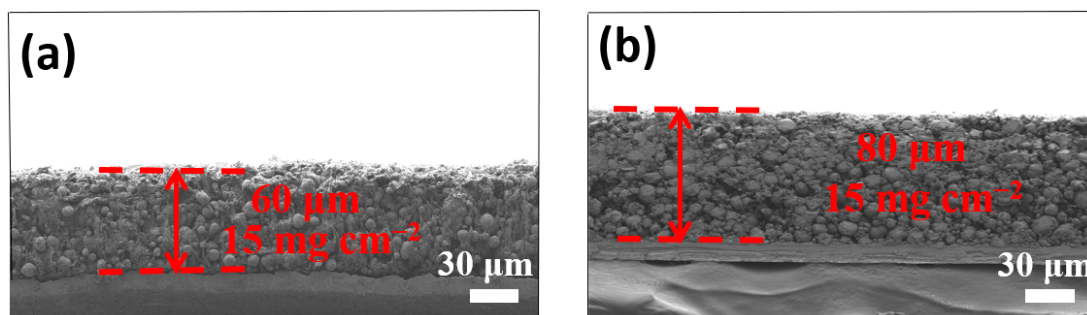


Figure 6. Cross-section SEM images of LRM with (a) dry film and (b) wet film.

SEM images of the cycled wet film section (Figure 7) showed obvious large voids, whereas SEM images of the dry film section did not have excessive pores, confirming the above illustration. Therefore, the choice of manufacturing process not only affects the structural integrity of the electrode but also plays a crucial role in determining the electrochemical performance and efficiency of the battery.

The comparative performance analysis between dry-processed and wet-processed electrodes conclusively demonstrates that LRM is highly prone to surface degradation (e.g., $Li_2CO_3/LiOH$ formation) and irreversible oxygen release when exposed to moisture or polar solvents during traditional slurry processing [34]. Therefore, dry processing, which eliminates solvent use, is suitable for the preparation of LRM electrodes. Furthermore, compared with commercially dominant cathode materials, such as lithium iron phosphate (LFP) and nickel–cobalt–manganese (NCM), as shown in Table S2 [27,35], LRM with a higher capacity (>250 mAh/g) demonstrate the potential of dry processing in enabling next-generation high-energy-density cathodes.

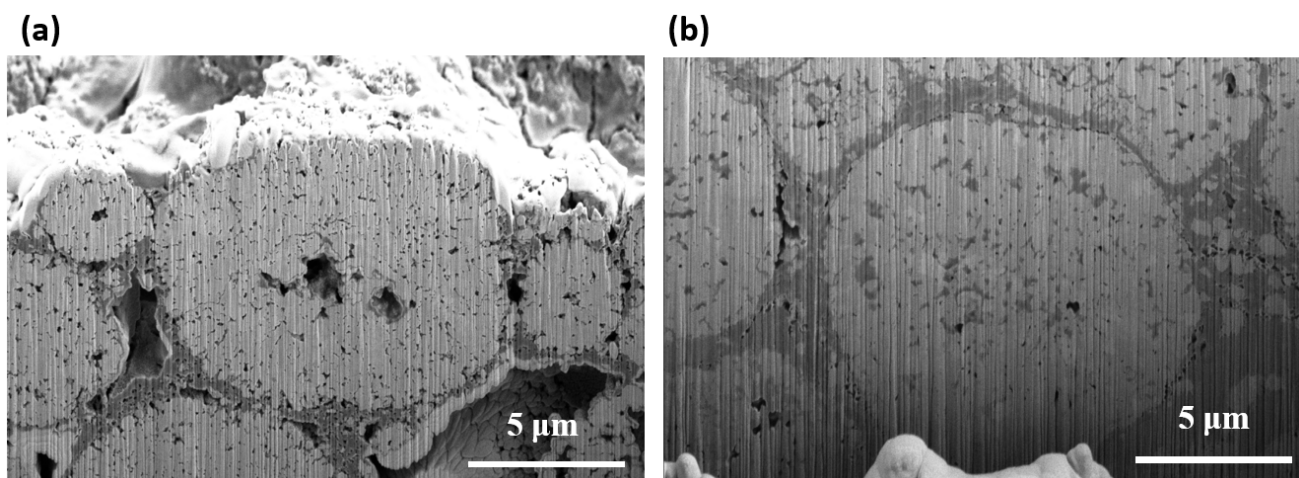


Figure 7. SEM image of cycled (a) wet film and (b) dry film.

4. Conclusions

This study successfully demonstrates the fabrication of lithium-rich manganese oxide (LRM) cathodes through an innovative dry binder fibrillation process. Through various morphologies of conductive carbon combinations, we established an optimized three-dimensional structure connected by points, lines, and surfaces for the cathodes. The structural design with close contact and tight packing improves the conductivity and facilitates more efficient e^-/Li^+ transport, ultimately resulting in enhanced battery performance. Comparing the electrochemical performance of dry electrodes with various thickness, a high areal capacity of 7.9 mAh cm^{-2} and a pouch cell with an energy density of 949 Wh kg^{-1} are achieved. The choice of manufacturing process also plays a crucial role in determining the performance. The dry film with a network structure optimizes the pathways for ion transport and electron conduction, leading to reduced resistance and superior coulombic efficiency and retention over cycling, potentially due to the more effective structural integrity and minimized side reactions during operation. In contrast, the wet film exhibits higher impedance due to clusters or a less uniform distribution of active materials and binders, which can hinder efficient e^-/Li^+ transfer and lead to increased side reactions with electrolytes. Therefore, this study proposed a practical strategy for designing lithium-rich manganese cathodes with high mass loading, aiming to address issues related to manufacturing processes. The design concept of building continuous interfaces and optimizing electrode structures can be applied to various cathodes to prepare high-mass-loading, long-life, and high-energy-density lithium-ion batteries, and can be further extended to sodium-ion batteries and beyond.

Supplementary Materials: The following supporting information can be downloaded at <https://www.mdpi.com/article/10.3390/batteries11040146/s1>; Supporting S1: Material preparation route; Figure S1: SEM image of internal structure of dry film; Figure S2: Electrical conductivity with different ratios of carbon; Figure S3: Comparison of XRD patterns between LRM raw materials and dry-processed electrodes; Figure S4: Compaction density and porosity of cathodes with different thicknesses; Figure S5: Cycling performance of cathodes with various mass loading at 0.1 C; Figure S6: Charge/discharge voltage profile of the Li metal pouch cell at 0.1 C; Figure S7: SEM image of wet film; Table S1: Film-forming properties and flexibility of electrodes with different material ratios. Table S2: Comparison of properties of different materials.

Author Contributions: Conceptualization, T.Y. and Z.W.; methodology, T.Y. and Z.W.; investigation, Y.M., H.G., T.Y. and Z.W.; data curation, Y.M., H.G., T.Y. and Z.W.; writing—original draft preparation, Y.M.; writing—review and editing, Y.M., T.Y. and Z.W.; visualization, Y.M., T.Y. and Z.W.; supervision,

Y.M., H.G., T.Y. and Z.W.; project administration, T.Y. and Z.W.; funding acquisition, Z.W. All authors have read and agreed to the published version of the manuscript.

Funding: This study was financially supported by the Science and Technology Program of Tianjin, China (24YDTPJC00140) and the Natural Science Foundation of Hebei Province, China (E2023202253).

Data Availability Statement: The data presented in this study are available upon request from the corresponding author.

Conflicts of Interest: The authors declare no conflicts of interest.

References

1. Sun, X.; Qin, C.L.; Zhao, B.Y.; Jia, S.F.; Wang, Z.F.; Yang, T.Z.; Liu, X.C.; Pan, L.N.; Zheng, L.L.; Luo, D.; et al. A cation and anion dual-doping strategy in novel Li-rich Mn-based cathode materials for high-performance Li metal batteries. *Energy Storage Mater.* **2024**, *70*, 103559. [[CrossRef](#)]
2. Xu, J.J.; Cai, X.Y.; Cai, S.M.; Shao, Y.X.; Hu, C.; Lu, S.R.; Ding, S.J. High-energy lithium-ion batteries: Recent progress and a promising future in applications. *Energy Environ. Mater.* **2023**, *6*, e12450. [[CrossRef](#)]
3. Wang, Z.F.; Yan, Y.J.; Zhang, Y.G.; Chen, Y.X.; Peng, X.Y.; Wang, X.; Zhao, W.M.; Qin, C.L.; Liu, Q.; Liu, X.J.; et al. Single-atomic Co-B₂N₂ sites anchored on carbon nanotube arrays promote lithium polysulfide conversion in lithium-sulfur batteries. *Carbon Energy* **2023**, *5*, e306. [[CrossRef](#)]
4. Yonaga, A.; Kawauchi, S.; Mori, Y.; Xuanchen, L.; Ishikawa, S.; Nunoshita, K.; Inoue, G.; Matsunaga, T. Effects of dry powder mixing on electrochemical performance of lithium-ion battery electrode using solvent-free dry forming process. *J. Power Sources* **2023**, *581*, 233466. [[CrossRef](#)]
5. Wang, Z.F.; Wang, H.Y.; Liu, X.L.; Chen, Y.X.; Zhao, Y.; Zhang, Y.G.; Han, Q.Q.; Qin, C.L.; Bakenov, Z.; Wang, Y.C.; et al. Single Zn atoms anchored on hollow carbon nanofiber network for dendrite-free lithium metal anode of flexible Li-S full cell. *Rare Met.* **2023**, *42*, 3705–3717. [[CrossRef](#)]
6. Arnot, D.J.; Mayilvahanan, K.S.; Hui, Z.; Takeuchi, K.J.; Marschilok, A.C.; Bock, D.C.; Wang, L.; West, A.C.; Takeuchi, E.S. Thick electrode design for facile electron and ion transport: Architectures, advanced characterization, and modeling. *Acc. Mater. Res.* **2022**, *3*, 472–483. [[CrossRef](#)]
7. Kuang, Y.; Chen, C.; Kirsch, D.; Hu, L. Thick electrode batteries: Principles, opportunities, and challenges. *Adv. Energy Mater.* **2019**, *9*, 1901457. [[CrossRef](#)]
8. Yao, W.; Chouchane, M.; Li, W.; Bai, S.; Liu, Z.; Li, L.; Chen, A.X.; Sayahpour, B.; Shimizu, R.; Raghavendran, G. A 5 V-class cobalt-free battery cathode with high loading enabled by dry coating. *Energy Environ. Sci.* **2023**, *16*, 1620–1630. [[CrossRef](#)]
9. Ryu, M.; Hong, Y.K.; Lee, S.Y.; Park, J.H. Ultrahigh loading dry-process for solvent-free lithium-ion battery electrode fabrication. *Nat. Commun.* **2023**, *14*, 1316. [[CrossRef](#)]
10. Kim, H.; Lim, J.H.; Lee, T.; An, J.; Kim, H.; Song, H.; Lee, H.; Choi, J.W.; Kang, J.H. Ozone-treated carbon nanotube as a conductive agent for dry-processed lithium-ion battery cathode. *ACS Energy Lett.* **2023**, *8*, 3460–3466. [[CrossRef](#)]
11. Tao, R.M.; Steinhoff, B.; Sun, X.G.; Sardo, K.; Skelly, B.; Meyer, H.M., III; Sawicki, C.; Polizos, G.; Lyu, X.; Du, Z.J.; et al. High-throughput and high-performance lithium-ion batteries via dry processing. *Chem. Eng. J.* **2023**, *471*, 144300. [[CrossRef](#)]
12. Sul, H.; Lee, D.; Manthiram, A. High-loading lithium-sulfur batteries with solvent-free dry-electrode processing. *Small* **2024**, *20*, 2400728. [[CrossRef](#)] [[PubMed](#)]
13. Gao, Y.N.; Yang, Y.; Yang, T.Z.; Zhang, Z.; Tang, L.; Mao, Z.Y.; Zhang, Y.G.; Luo, D.; Chen, Z.W. Design lithium exchanged zeolite based multifunctional electrode additive for ultra-high loading electrode toward high energy density lithium metal battery. *Adv. Energy Mater.* **2024**, *15*, 2403063. [[CrossRef](#)]
14. Lv, Z.W.; Liu, J.; Li, C.; Peng, J.X.; Zheng, C.X.; Zheng, X.F.; Wu, Y.Q.; Xia, M.; Zhong, H.Y.; Gong, Z.L.; et al. High-areal-capacity all-solid-state Li-S battery enabled by dry process technology. *Etransportation* **2024**, *19*, 100298. [[CrossRef](#)]
15. Fu, J.Z.; Gong, X.T.; Jin, W.T.; Podder, C.; Liu, Y.T.; Yang, Z.Z.; Sultanov, M.; Pan, H.; Wang, Y. Enable superior performance of ultra-high loading electrodes through the cost-efficient solvent-free electrode manufacturing technology. *Energy Storage Mater.* **2024**, *69*, 103423. [[CrossRef](#)]
16. Lu, Y.; Zhao, C.Z.; Yuan, H.; Hu, J.K.; Huang, J.Q.; Zhang, Q. Dry electrode technology, the rising star in solid-state battery industrialization. *Matter* **2022**, *5*, 876–898. [[CrossRef](#)]
17. Tang, W.H.; Zhu, J.P.; Chen, C.; Ye, Q.; Zeng, F.H.; Ma, Z.P. Modification strategies and challenges of high-performance lithium-rich manganese-based cathode materials. *Energy Technol.* **2024**, *12*, 2301254. [[CrossRef](#)]
18. Li, Q.; Yang, Y.; Yu, X.Q.; L, H. A 700 W·h·kg⁻¹ rechargeable pouch type lithium battery. *Chin. Phys. Lett.* **2023**, *40*, 048201. [[CrossRef](#)]

19. Yuan, X.D.; Dong, T.; Liu, J.X.; Cui, Y.Y.; Dong, H.T.; Yuan, D.; Zhang, H.T. Biaffinity electrolyte optimizing high-voltage lithium-rich manganese oxide battery via interface modulation strategy. *Angew. Chem. Int. Ed.* **2023**, *62*, e202304121. [[CrossRef](#)]
20. Zhang, B.D.; Wu, X.H.; Luo, H.Y.; Yan, H.; Chen, Y.L.; Zhou, S.Y.; Yin, J.H.; Zhang, K.; Liao, H.G.; Wang, Q.S.; et al. Gradient interphase engineering enabled by anionic redox for high-voltage and long-life Li-ion batteries. *J. Am. Chem. Soc.* **2024**, *146*, 4557–4569. [[CrossRef](#)]
21. Ge, B.C.; Deng, J.J.; Wang, Z.J.; Liang, Q.H.; Hu, L.; Ren, X.Y.; Li, R.M.; Lin, Y.X.; Li, Y.S.; Wang, Q.R.; et al. Aggregate-dominated dilute electrolytes with low-temperature-resistant ion-conducting channels for highly reversible Na plating/stripping. *Adv. Mater.* **2024**, *36*, 2409161. [[CrossRef](#)] [[PubMed](#)]
22. Steven, L.; Su, L.S.; Alex, M.; Cui, Z.H.; Arumugam, M. Cracking vs. surface reactivity in high-nickel cathodes for lithium-ion batteries. *Joule* **2023**, *7*, 2430–2444.
23. Wade, A.; Llewellyn, A.V.; Heenan, T.M.M.; Tan, C.; Brett, D.J.L.; Jervis, R.; Shearing, P.R. First cycle cracking behaviour within Ni-rich cathodes during high-voltage charging. *J. Electrochem. Soc.* **2023**, *170*, 070513. [[CrossRef](#)]
24. Gao, T.H.; Andrew, K.; Lu, W. Modeling electrode-level crack and quantifying its effect on battery performance and impedance. *Electrochim. Acta* **2020**, *363*, 137197. [[CrossRef](#)]
25. Xu, M.; Reichman, B.; Wang, X. Modeling the effect of electrode thickness on the performance of lithium-ion batteries with experimental validation. *Energy* **2019**, *186*, 115864. [[CrossRef](#)]
26. An, F.Q.; Zhou, W.N.; Li, P. A comparison of model prediction from P2D and particle packing with experiment. *Electrochim. Acta* **2021**, *370*, 137775.
27. Kwon, K.; Kim, K.; Han, S.; Lee, J.; Lee, H.; Kwon, J.; Lee, J.; Seo, J.; Kim, P.J.; Song, T.; et al. Low-resistance LiFePO₄ thick film electrode processed with dry electrode technology for high-energy-density lithium-ion batteries. *Small Sci.* **2024**, *4*, 2300302. [[CrossRef](#)]
28. Liang, J.W.; Zhu, Y.M.; Li, X.N.; Luo, J.; Deng, S.X.; Zhao, Y.; Sun, Y.P.; Wu, D.J.; Hu, Y.F.; Li, W.H.; et al. A gradient oxy-thiophosphate-coated Ni-rich layered oxide cathode for stable all-solid-state Li-ion batteries. *Nat. Commun.* **2023**, *14*, 146. [[CrossRef](#)]
29. Chen, D.C.; Kan, W.H.; Chen, G.Y. Understanding performance degradation in cation-disordered rock-salt oxide cathodes. *Adv. Energy Mater.* **2019**, *9*, 1901255.
30. Bai, P.X.; Ji, X.; Zhang, J.X.; Zhang, W.R.; Hou, S.; Su, H.; Li, M.J.; Deng, T.; Cao, L.S.; Liu, S.F.; et al. Formation of LiF-rich cathode-electrolyte interphase by electrolyte reduction. *Angew. Chem. Int. Ed.* **2022**, *61*, e202202731. [[CrossRef](#)]
31. Feng, Z.R.; Guo, L.Y.; Liu, X.F.; Li, W.W.; Zhang, R.P.; Wang, D.; Zhang, W.; Zheng, W.T. Stabilizing the lithium-rich manganese-based oxide cathode via regulating a CEI film. *ACS Appl. Energy Mater.* **2024**, *7*, 2791–2799. [[CrossRef](#)]
32. Li, A.L.; Li, G.H.; Lu, S.G.; Ren, Z.M.; Wang, J.T.; Zhuo, H.X.; Quan, W.; Zhang, G.N.; Han, F.J.; Xia, Y.M.; et al. Interface stabilization of 1,1,2,2-tetrafluoroethyl-2,2,3,3-tetrafluoropropyl ether to high-voltage Li-rich Mn-based layered cathode materials. *Rare Met.* **2022**, *41*, 822–829. [[CrossRef](#)]
33. Beuse, T.; Fingerle, M.; Wagner, C.; Winter, M.; Boerner, M. Comprehensive Insights into the Porosity of Lithium-Ion Battery Electrodes: A Comparative Study on Positive Electrodes Based on LiNi_{0.6}Mn_{0.2}Co_{0.2}O₂ (NMC622). *Batteries* **2021**, *7*, 70. [[CrossRef](#)]
34. Li, Q.H.; Wang, Y.; Wang, X.L.; Sun, X.R.; Zhang, J.N.; Yu, X.Q.; Li, H. Investigations on the fundamental process of cathode electrolyte interphase formation and evolution of high-voltage cathode. *ACS Appl. Mater. Interfaces* **2019**, *12*, 2319–2326. [[CrossRef](#)]
35. Wu, F.; Shi, Q.; Chen, L.; Dong, J.; Zhao, J.; Wang, H.; Gao, F.; Liu, J.; Zhang, H.; Li, N.; et al. New insights into dry-coating-processed surface engineering enabling structurally and thermally stable high-performance Ni-rich cathode materials for lithium ion batteries. *Chem. Eng. J.* **2023**, *470*, 144045. [[CrossRef](#)]

Disclaimer/Publisher’s Note: The statements, opinions and data contained in all publications are solely those of the individual author(s) and contributor(s) and not of MDPI and/or the editor(s). MDPI and/or the editor(s) disclaim responsibility for any injury to people or property resulting from any ideas, methods, instructions or products referred to in the content.